

Pressure-dependent structures of amorphous red phosphorus and the origin of the first sharp diffraction peaks

JOSEPH M. ZAUG^{1*}, ALAN K. SOPER² AND SIMON M. CLARK^{3,4}

¹Chemistry Materials Energy and Life Sciences, Lawrence Livermore National Laboratory, 7000 E. Avenue, L-350, Livermore, California 94551, USA

²ISIS Facility, STFC Rutherford Appleton Laboratory, Harwell Science and Innovation Campus, Didcot, OX11 0QX, UK

³Advanced Light Source, Lawrence Berkeley Laboratory, Berkeley, California 20015, USA

⁴Department of Earth and Planetary Sciences, University of California, Berkeley, California 94720, USA

*e-mail: zaug1@llnl.gov

Published online: 12 October 2008; doi:10.1038/nmat2290

Characterizing the nature of medium-range order (MRO) in liquids and disordered solids is important for understanding their structure and transport properties. However, accurately portraying MRO, as manifested by the first sharp diffraction peak (FSDP) in neutron and X-ray scattering measurements, has remained elusive for more than 80 years. Here, using X-ray diffraction of amorphous red phosphorus compressed to 6.30 GPa, supplemented with micro-Raman scattering studies, we build three-dimensional structural models consistent with the diffraction data. We discover that the pressure dependence of the FSDP intensity and line position can be quantitatively accounted for by a characteristic void distribution function, defined in terms of average void size, void spacing and void density. This work provides a template to unambiguously interpret atomic and void-space MRO across a broad range of technologically promising network-forming materials.

The functional versatility of non-crystalline materials has enabled revolutionary technological advances. Examples include amorphous silicon, an important component of solar cells¹ and flat-panel displays²; chalcogenide glasses such as Ge₂Sb₂Te₅, which are used in novel storage devices including optical DVDs (ref. 3); and nanolaminates such as copper–zirconium glass, which significantly enhances the plasticity of crystalline materials⁴. And yet, unlike crystalline material characterizations, the molecular functions of disordered materials are not definitively correlated with atomic structure, which hinders systematic engineering routes towards advanced materials design. Although non-crystalline materials do not exhibit long-range order, they can exhibit medium-range order⁵ (MRO) on the scale of 5–20 Å. Atomic structures are typically quantified in terms of site–site pair-distribution functions (PDFs) $g(r)$, which provide probabilities for nearest-neighbour bond distances, bond angles and bonding coordination numbers. Nevertheless, in the absence of theory, these provide an insufficient basis to confidently identify intrinsic building-block structures.

To capture the underlying physics that accounts for novel MRO materials properties, compelling explanations have been sought to quantifiably link observed first sharp diffraction peak (FSDP) attributes to medium-range atomic-scale architectures. The FSDP intensity, occurring at scattering vector values $Q < 2 \text{ \AA}^{-1}$, is thought to indicate the degree of atomic MRO. The origin of the FSDP has been attributed to numerous models, including nanovoids intrinsic to continuous-random network (CRN) ring structure topologies⁶, interstitial-void correlations concurrent with bond directionalities induced by chemical ordering⁷ (the

concentration–concentration partial structure factor, $S_{cc}(Q)$ in the Bhatia–Thornton formalism⁸), separations between CRN inter-layered structures^{9–15}, cation–cation correlations¹⁶, long-range atomic correlations¹⁷, zones of low atomic occupancy¹⁸, transient atomic layered void separations¹⁴, cluster correlations¹⁹ and density deficits induced by loan-pair interactions¹⁵. Complications arise when developing MRO structural models using sparsely tested restrictions, which result because the FSDP origin is ambiguous or misinterpreted. For example, the notion that chemical ordering induces voids, and thus accounts for the origin of FSDPs, implies rigid geometrical bonding restrictions that are feasibly untenable when considering MRO network fluids well above glass-transition temperatures or monatomic systems where $S_{cc}(Q)$ contributions to the total scattering function, $S(Q)$, are respectively very weak and absent.

Amorphous red phosphorus (a-rP) is an archetypal MRO semiconductor. The atomic PDF and average atomic properties were first reported in 1935 by Hultgren, Gingrich and Warren²⁰. Experimental efforts conducted on conventionally made a-rP since 1967 include X-ray diffraction^{10,21,22}, infrared absorption^{11,12}, Raman spectroscopy^{11,23,24}, photo-induced electron-spin resonance²⁵, electrical conductivity^{26–28}, photoluminescence²⁹, optically detached magnetic resonance³⁰, neutron diffraction^{31–34}, extended X-ray absorption fine structure³⁵, X-ray photoemission spectroscopy¹³ and transmission electron micrographic studies³⁶. However, a description of solid-state a-rP structural subunits where theory and experimental data agree has remained unsolved. Theoretical initiatives carried out *in silico* include force-constant models³⁷, molecular dynamic density functional

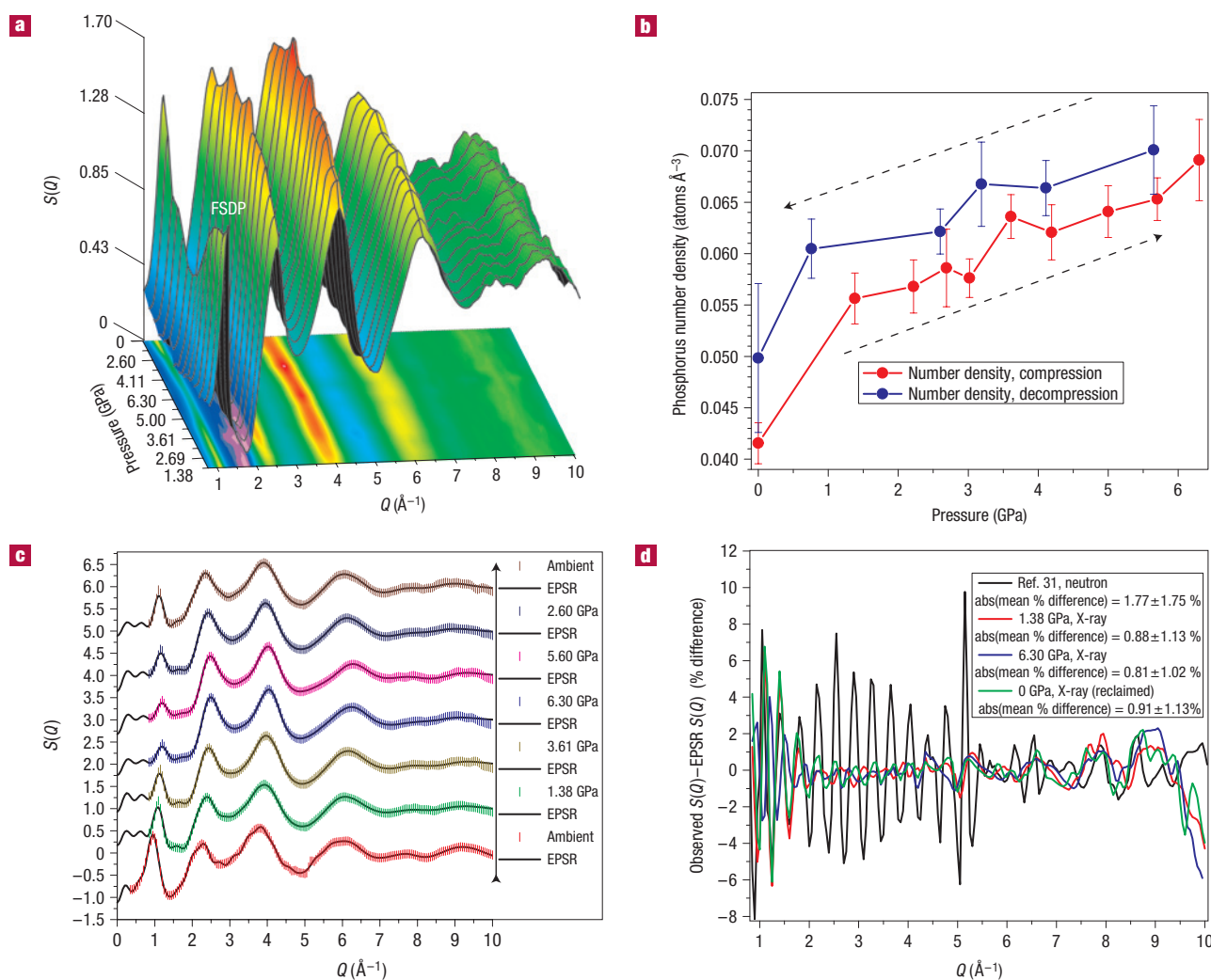


Figure 1 Atomic number densities are computed from total scattering function results and these parameters constrain structurally refined models that compare extremely well to X-ray diffraction results. Total scattering function data, where $Q_{\text{max}} > 8\text{--}10 \text{\AA}^{-1}$, are required to compute atomic number densities with $\pm 3\text{--}5\%$ error; $S(Q)$ and ρ guide the development of structural models using the EPSR method. **a**, FSDP intensity correlates strongly with pressure. Increasing pressure also shifts the line position to higher Q . Here, the a-rP $S(Q)$ contour begins at 1.38 GPa. Hydrostatic pressure is applied up to 6.30 GPa and then pressure is systematically released. **b**, Computed a-rP number densities plotted along the compression cycle (red circles) and decompression cycle (blue circles). The ambient pressure value represents the average of three helium pycnometry measurements. Error bars represent the standard deviation of 20 separate computations from $S(8\text{--}10 \text{\AA}^{-1})$ data. The bulk modulus is determined to be 5 ± 1 GPa using the Birch–Murnaghan equation-of-state model where K'_0 is fixed at 4.0. As pressure is released density drops, although a complete recovery to the precompression value requires thermal heating of the reclaimed sample. Here, the reclaimed a-rP density is 20% higher than the precompressed value. **c**, A selection of EPSR model results (solid black lines) with corresponding X-ray diffraction results (coloured vertical lines). Data are vertically offset to enhance clarity. The ambient-pressure neutron data at the bottom of the plot are from Elliott *et al.*³¹. **d**, Residual differences between X-ray and model $S(Q)$ data are typically $\pm \sim 2\%$, whereas $\pm 5\text{--}10\%$ oscillations occur in the ambient-pressure neutron data below $Q = 5 \text{\AA}^{-1}$ and then fall to $< 2\%$ from 5.5 to 30 \AA^{-1} .

theory methods^{38,39}, *ab initio* self-consistent field and second-order Møller–Plesset calculations⁴⁰, full-potential linear muffin-tin orbital molecular dynamics⁴¹ and reverse Monte Carlo simulations^{3,34}. Constructed theoretical models essentially fall into three paradigms: (1) CRN models consisting of layered structures^{10–12,42} (2) tubular or chain-like structures^{24,36,37,40} often consisting of pentagonal rings and (3) a distribution of n-member clusters^{38–41}. Thus far, no theoretical construct yields a physically plausible three-dimensional (3D) a-rP architecture that definitively matches X-ray and/or neutron scattering measurements. Here, we present an integrated study using our laboratory results to constrain our empirical potential structure refinement (EPSR)

computations and corresponding void structure analysis of a prototypical MRO material. These analysis tools can be applied to accurately characterize 3D atomic and void structures within multi-atomic network-forming materials.

We carry out ambient-temperature X-ray diffraction and micro-Raman spectroscopy measurements on hydrostatically compressed and decompressed a-rP up to a maximum pressure of 6.30 GPa. Experimental structure factors $S(Q)$ are shown in Fig. 1a. Using $S(Q)$ data, atomic number densities, ρ , are computed and pressure-dependent values are given in Table 1 and plotted in Fig. 1b. $S(Q)$ and ρ values constrain refinements of atomic structural models using the EPSR method⁴³

Table 1 Densities, first-nearest-neighbour coordination and nearest-approach values and void fractions determined in this study. Density was determined from the slope of the intramolecular region of the electron density partial structure factor $F(r)$ (ref. 49). At each pressure, the first peak in $g(r)$ was integrated up to the first minimum given by r_{\min} to yield the corresponding coordination number for nearest-neighbour phosphorus atoms. The total void fraction within our EPSR simulation box, f_v , is simply the ratio of the number of void pixels divided by the total pixel number (10^6). An occupied pixel criterion is set by r_{\max} , the assumed nearest-approach distance of atoms given by the first peak maximum position in $g(r)$. Any pixel position $> r_{\max}$ away from local phosphorus atoms is assigned as unoccupied.

Pressure (GPa)	Density (atoms \AA^{-3})	r_{\min} (\AA)	Coordination number	r_{\max} (\AA)	f_v
0	0.0416	2.92	3.8	2.22	0.1067
Elliott					
1.38	0.0526 (0.0023)	2.75	4.3	2.18	0.0510
2.22	0.0565 (0.0023)	2.76	4.6	2.18	0.0429
2.69	0.0583 (0.0034)	2.76	4.6	2.18	0.0338
3.02	0.0594 (0.0017)	2.76	4.6	2.18	0.0215
3.61	0.0610 (0.0019)	2.76	4.6	2.18	0.0204
4.19	0.0624 (0.0024)	2.75	4.5	2.18	0.0057
5.00	0.0641 (0.0023)	2.73	4.5	2.18	0.0041
5.70	0.0657 (0.0019)	2.71	4.5	2.18	0.0020
6.30	0.0670 (0.0036)	2.70	4.5	2.18	0.0013
5.65	0.0701 (0.0039)	2.68	4.6	2.13	0.0016
4.11	0.0676 (0.0024)	2.72	4.7	2.18	0.0009
3.19	0.0655 (0.0037)	2.71	4.6	2.20	0.0027
2.60	0.0639 (0.0020)	2.74	4.5	2.20	0.0025
0.76	0.0567 (0.0026)	2.76	4.2	2.22	0.0176
0	0.0498 (0.0065)	2.76	3.5	2.24	0.0248

(Fig. 1c). The residual difference between our X-ray data and simulated structure factors is typically less than 2% (Fig. 1d). Here, well-constrained EPSR $S(Q)$ values yield model PDFs that agree very well with experimental data (Fig. 2a, Supplementary Information, Fig. S1a,b). Constrained EPSR $g(r)$ data enable a rigorous and comprehensive interpretation of 3D MRO structures; this high degree of analysis cannot be achieved using experimental PDFs alone. Pressure-dependent Raman spectra and corresponding line positions are provided in Supplementary Information, Fig. S2a–c. We also investigate thermal heating effects on ambient-pressure-reclaimed a-rP (Supplementary Information, Fig. S3).

A principle discovery of this study is that a-rP comprises P_3 triangles and P_4 pyramidal subunit structures linked by chains of P atoms. Structural models match experimental PDF data when we permit P_3 triangles and P_4 pyramids to form in the EPSR simulations. Indeed, evidence suggests these structures exist in red phosphorus^{23,35}. It is not possible to match PDF data by assuming a purely tetrahedral local coordination (P_4 units) because the second peak position in $g(r)$ is at too low an r -value to permit strictly tetrahedral coordination. Hence, the present model, consisting of P_3 triangles and P_4 pyramids linked by chains of P atoms is the only one consistent with neutron diffraction data³¹. If undistorted tetrahedrally bonded subunit structures were to occur, then P–P–P bond angles should occur in the vicinity of 109° – 110° . The PDF data indicates the average P–P–P angle varies from 103° at ambient conditions to 98° at 6.30 GPa (Fig. 2b,c). Moreover, we find the ambient-condition coordination of a-rP, calculated from the area under the first EPSR peak in $g(r)$, to be nearly four-fold with a value of 3.8, which is common among tetraelemental elements.

Our consideration of P_3 triangles presumes two P atoms to be bonded if their neighbour distances are less than or equal to the first minimum well spacing in $g(r)$, r_{\min} (values listed in Table 1). Here, the second peak in $g(r)$ implies a P–P–P bond angle centred about 100° , evident of a covalent bonding network. Hence, we might surmise that purely tetrahedral bonding coordination (for example, Si, Ge), if it exists in a-rP, is much less probable

(that is, the probability distribution between 106° and 112° bond angles is less than the 100° distribution). The data shown in Fig. 2 clearly indicate a strong propensity for the existence of P_3 triangles including P_4 pyramids, both structures contributing bond-angle peak distributions near 60° . The average atomic positions (Fig. 3a) suggest that links to these and other such subunit structures result in the more diffuse bond-angle distribution near 151° . The distribution centred near 100° is attributed to links between second-nearest neighbours within winding chains of P atoms that connect triangular P_3 and/or pyramidal P_4 subunits. To further check the integrity of our model, we truncated Elliott's $S(Q)$ from 30 \AA^{-1} down to 10 \AA^{-1} and the resultant analysis of $g(r)$ yields no change in the angular distribution peak positions used to construct our 3D structural model (see Supplementary Information, Fig. S4).

There are clear and significant structural correlations that extend beyond the spatial range of our potential surface or simulation box length (30 \AA) as evident by low-amplitude truncation oscillations in EPSR $S(Q)$ values at $Q < 1.8 \text{ \AA}^{-1}$. In addition, the ambient-pressure data of Elliott *et al.*³¹ have markedly reduced peak line positions compared with our 0.01 GPa X-ray data (see Supplementary Information, Fig. S5). The FSDP intensity from neutron scattering is 24% less and the area is about 20% more than the X-ray result and in part this may be due to differences in wavelength-dependent scattering efficiency and/or sample porosity. Unfortunately our 0.01 GPa data extends to only $Q = 5.8 \text{ \AA}^{-1}$ and consequently, large-amplitude Fourier-transform truncation oscillations decimated the integrity of $g(r)$. Extrapolating trends observed in higher Q -range and pressure-range X-ray results to ambient pressure indicate our sample has a $+5^\circ$ distribution of P–P–P diffuse bond angles and a corresponding 18% increase in probability. Putting the differences in neutron and X-ray $S(Q)$ values aside, a more illuminated picture of MRO structural networks is revealed by studying effects driven by hydrostatically applied pressure.

When pressure is applied, the electrical resistivity of a-rP falls by nine orders in magnitude; this effect was observed by Extnance and Elliott²⁷ in 1980. Does an anomalous relationship exist between electrical transport and the nature of MRO in network-forming

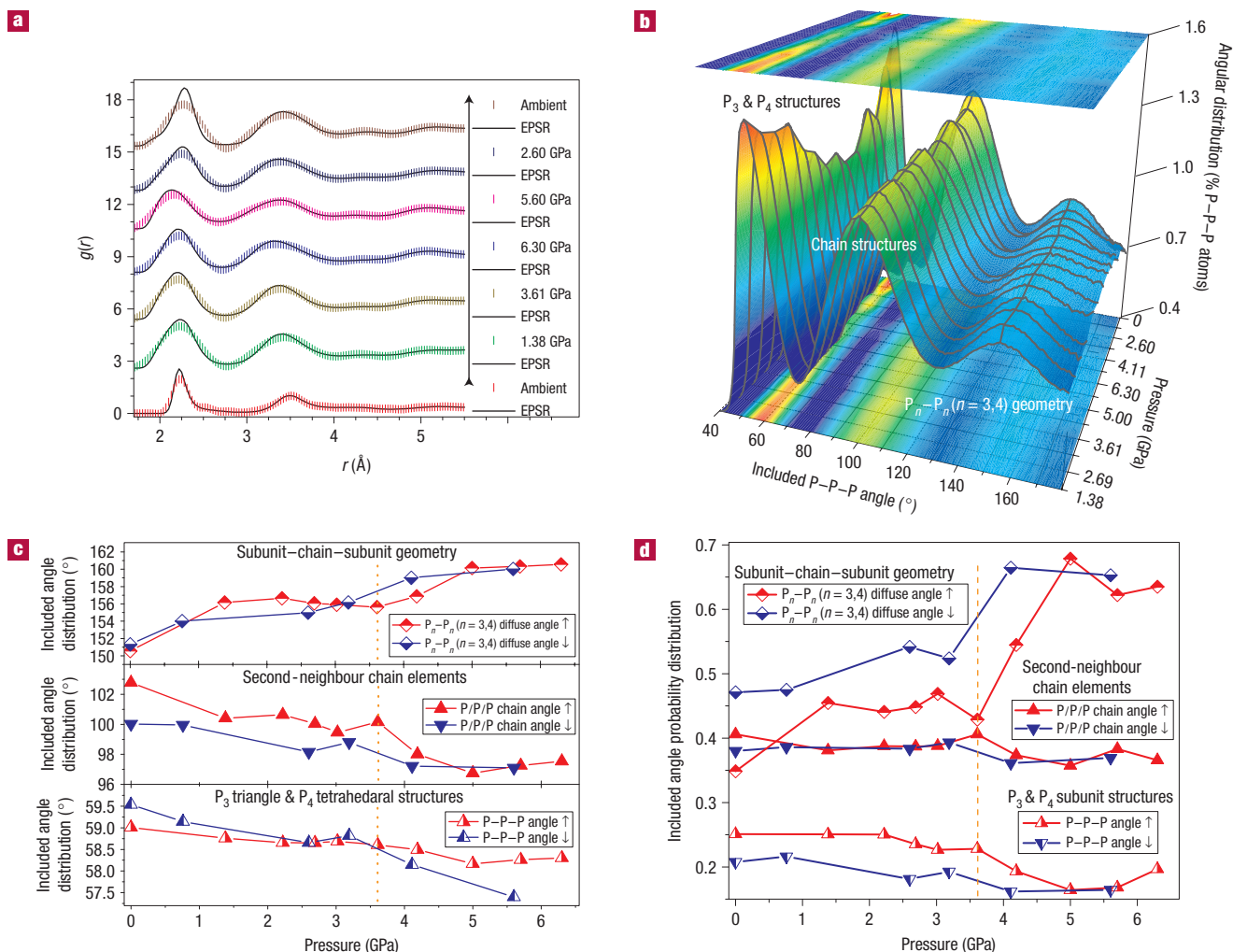


Figure 2 Experimentally constrained structural refinement models provide a means to plausibly discern 3D MRO atomic structures. Here, our modelled PDF data provide a much more rigorous basis to elucidate MRO a-rP structures than experimental data alone. **a**, A selection of modelled $g(r)$ results (solid black lines) compared against Fourier-transformed experimental $S(Q)$ data (coloured vertical lines). X-ray results are shifted vertically to ease comparison. (A contour plot of PDF data from $Q = 5.0\text{--}7.0\text{ \AA}^{-1}$ is shown in Fig. 3b.) The ambient-pressure neutron and model PDFs are scaled down by a factor of 0.4. The neutron PDF exhibits narrowed peaks as a consequence of Fourier transforming $S(Q)$ data extending out to $Q = 30\text{ \AA}^{-1}$ (not shown). **b**, A contour of bond-angle distributions where the P–P bond length is assumed to be the pressure-dependent first-nearest-neighbour distance, r_{max} , given by the first peak position in modelled PDFs. **c**, The included angle positions for each prominent angular distribution plotted to show compression (red plot symbols \uparrow) and decompression (blue plot symbols \downarrow) cycles. The most significant pressure-induced change occurs between 3.61 and 5.00 GPa where connected P_3 triangles and/or P_4 pyramids begin to open up as signalled by the 5.6° increase in the broad peak initially centred at 150.6° . These trends reverse, although not completely, on release of pressure. **d**, Included angle probability distributions indicate P_3 and P_4 structures diminish by approximately 22%. There is an 11% reduction in second-nearest-neighbour chain elements, and more importantly, these axial components become more compact, as is evident by the corresponding 5.3° reduction in angular distribution. Most striking is a 58% rise (from 3.61–5.00 GPa) in the distribution of network-connected P_3 triangles and/or P_4 pyramids. Above 3.61 GPa, the relative number of these more flattened chain-linked structures dominates the topology of a-rP.

semiconductors? We see an inverse relation between FSDP intensity and pressure (Fig. 1a). At 0.01 GPa, the FSDP line position is $1.077(1)\text{ \AA}^{-1}$ and at 6.30 GPa, it is shifted by only $+0.129\text{ \AA}^{-1}$. Likewise, localized bond lengths change very little as reflected by the fact that the Raman scattering peak positions shift only $<0.3\text{ cm}^{-1}\text{ GPa}^{-1}$. However, there are significant changes to non-localized vibrational peak intensity ratios (see Supplementary Information, Fig. S2a). The first- and second-nearest-neighbour PDF peaks are displaced by only -0.010 and -0.170 \AA respectively (Fig. 3a). The nearest-neighbour coordination number is virtually invariant to compression (Table 1) while the ambient pressure

ρ increases 66%. Pressure has little effect on short-range-order correlation lengths and the P_3 and P_4 structures that remain at 6.30 GPa are not significantly deformed.

The most significant structural changes occur above $r = 5\text{ \AA}$, where MRO nearest-neighbour peaks present at high pressure are generally much weaker and poorly defined at the lower densities (Fig. 3b). A strong pressure-dependent correspondence appears between the sixth-, seventh- and eighth-nearest-neighbour peak positions and the most intense intermolecular Raman peak ($350.8 \pm 1\text{ cm}^{-1}$ at ambient pressure); starting at ambient pressure, all three line positions steadily decline in magnitude until

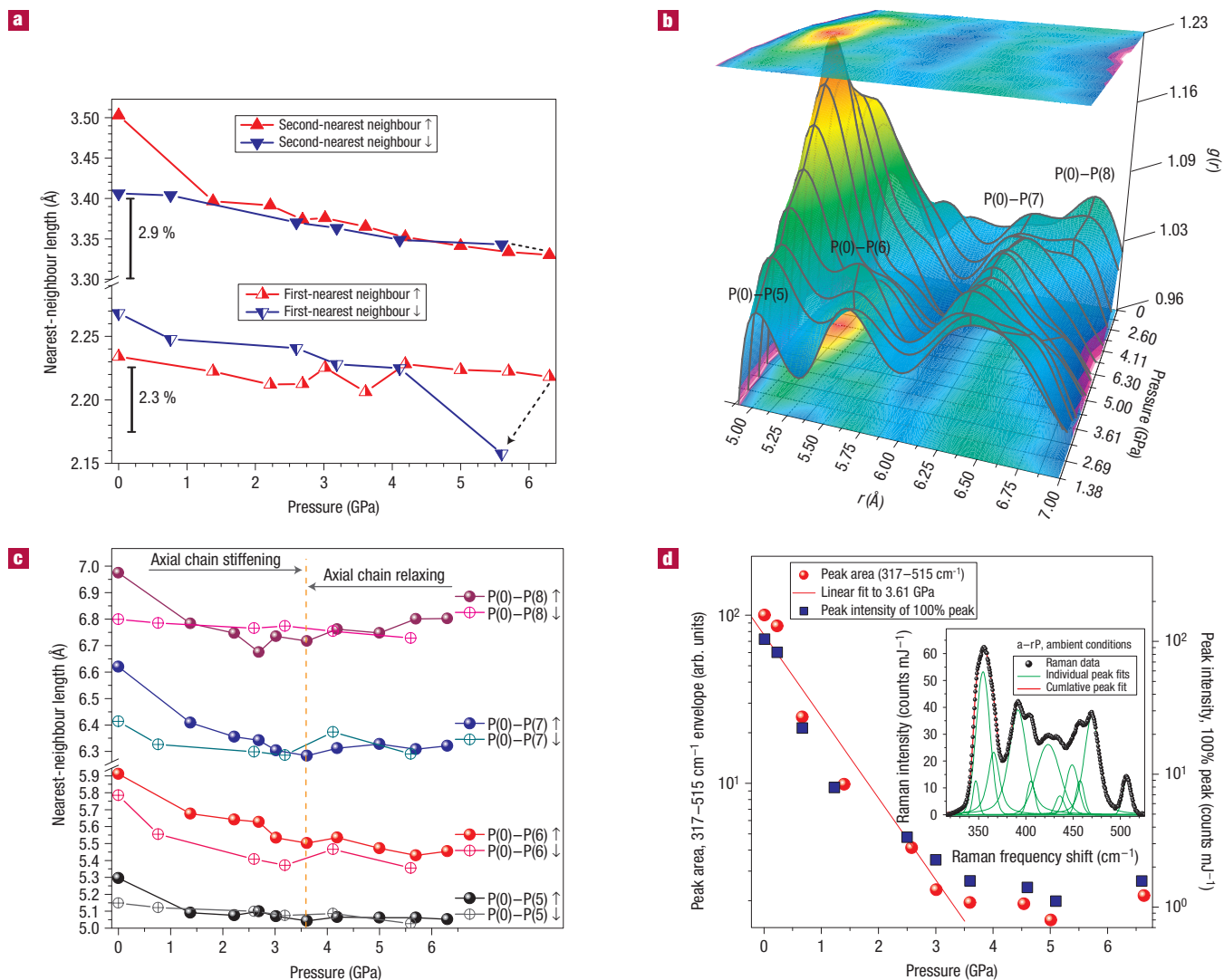


Figure 3 When pressure is applied, winding phosphorus chains contract up to 3.61 GPa, where connected subunit structures then separate from each other and buckle into surrounding space. **a**, The first- and second-nearest-neighbour $g(r)$ peak positions plotted across compression (upward directed red triangles \uparrow) and decompression (downward directed blue triangles \downarrow) cycles. These short-range-order coordination lengths are virtually unaffected by pressure. The relatively high second-nearest-neighbour length at ambient pressure may indicate a difference between our sample and that of Elliott *et al.*³¹ **b,c**, The sixth- to eighth-nearest-neighbour coordination lengths reflect a high degree of sensitivity to applied pressure. At 3.61 GPa, the fifth-nearest-neighbour peak, P(5), area has increased to five times the ambient value, suggesting an anomalous inverse relationship to FSDP intensity. The sixth, seventh and eighth coordination shell lengths decrease from ambient to 3.61 GPa, where suddenly this trend stops. These trends reflect the degree of axial compression along specific components of the a-rP chain network. Above 3.61 GPa, the seventh- and eighth-nearest-neighbour lengths now increase, suggesting a possible association with the buckling diffuse bond-angle structures. **d**, These trends are corroborated by our micro-Raman spectroscopy results. Raman peaks are highly convoluted (inset); however, relative signal intensity and peak areas are determined with high precision. The initial high signal strength is attributed to a resonant Raman effect. Here, the HeNe laser excitation energy nearly matches the a-rP bandgap energy. A 10^2 loss in Raman signal intensity from ambient to 3.61 GPa is ascribed to a pressure-induced closure of the electronic bandgap. Extance and Elliott attribute an abrupt drop in electrical resistance at 35 kbar (3.5 GPa) to a change in conduction mechanisms²⁷. Our atomic structure models thus indicate that buckling chain-linked P_3 and/or P_4 subunit structures draw non-bonding orbitals more closely together, thereby changing the density of defect states.

3.61 GPa, where suddenly these progressions terminate (Fig. 3c and Supplementary Information, Fig. S2c). Redshifting of this Raman mode indicates a decrease in vibrational interaction length between similar subunit structures. We interpret these parallel trends as a stiffening of longitudinal displacement along axial chain components where the effects of compression are most pronounced. This raises the question: why, in an amorphous material, should there be a sudden decrease in the compressibility

of a MRO structural network, whereas more localized bonds remain apparently unaffected by pressure?

Between 3.61 and 5.00 GPa, there is a noteworthy 58% jump in the distribution probability of diffuse bond angles (Fig. 2d), and coincidentally, the resonant Raman effect abruptly terminates (Fig. 3d). One precursor to these striking events is the extinction of three Raman modes at 3.00 GPa. Between 3.00 and 3.61 GPa, there seems to be a ‘tipping point’ where longitudinal chain components

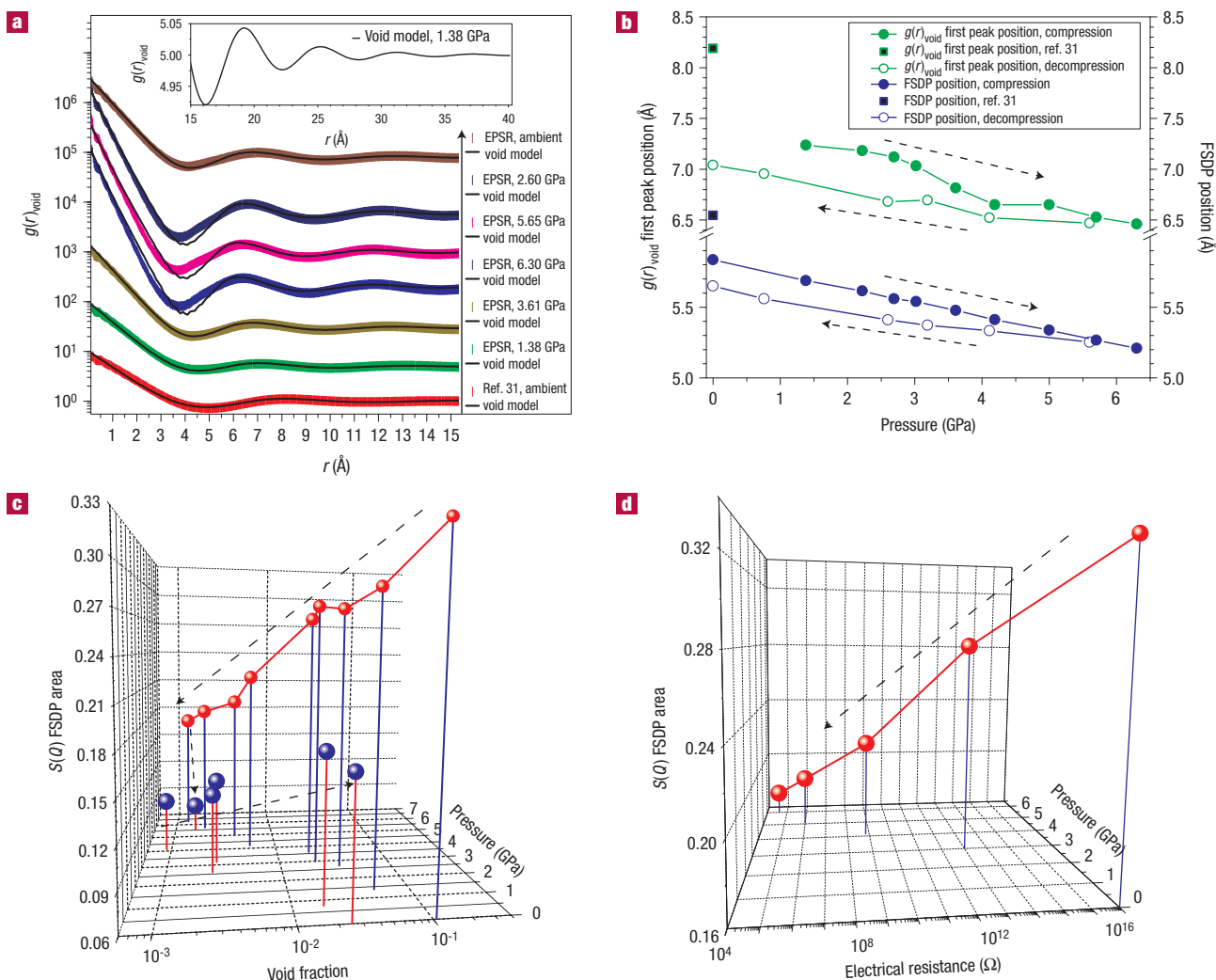


Figure 4 Calculated void-pixel pair distribution functions and a model for $g(r)_{\text{void}}$ quantitatively tie FSDP attributes to average void size, void spacing and void density. **a**, A selection of computed void-pixel pair-distribution functions derived from highly partitioned EPSR boxes (coloured vertical lines) plotted with results from a $g(r)_{\text{v}}$ model (solid black lines). The EPSR empirical potential used was cut off at 18 Å thus limiting the range of calculated void-pixel distributions. The model is a convolution of a void-particle distribution function, $g_p(r)$, with a pair distribution of void centres, $g_c(r)$, incorporating a hard-sphere diameter, R_c , given by the Percus–Yevick function. The rise at low r is effectively the inverse of the void fraction, $1/r_v$. Curves are shifted vertically to facilitate comparison. The example inset figure shows that void-space oscillations extend well beyond the 30 Å dimension of the EPSR box. **b**, The first peak position in $g(r)_{\text{void}}$ plotted along compression (filled circles) and decompression (open circles) cycles compared to $2\pi/Q_{\text{FSDP}}$. The pressure-dependent factors of $Q_{\text{FSDP}}g(r)_{\text{void}}$ -1st pk and $Q_{\text{FSDP}}R_c$ are nearly constant, suggesting a strong interdependent correlation between the FSDP line position, average void size and void spacing (Table 2). **c**, The FSDP area as a function of void fraction along compression (red spheres) and decompression (blue spheres) cycles. The linear response of the FSDP scattering intensity to void fraction implies a strong interdependent correlation between FSDP area and void density. **d**, The pressure-dependent FSDP area as a function of electrical resistance measured by Extance and Elliott²⁷. The ambient-pressure resistance value is determined by extrapolating their data. The linear relation between FSDP scattering intensity and electrical conductivity exhibits a highly correlated anomalous behaviour. Is this phenomenon unique to a-rP?

stiffen up and subsequent increases in pressure force connected P_3 and/or P_4 subunit links to separate and buckle into surrounding space. Above 5.00 GPa, these deformed chain-linked structures stiffen significantly until at 6.60 GPa there is a phase transition to crystalline black phosphorus (see Supplementary Information, Fig. S6a,b) These atomic-scale transitions underscore the changes observed on the macroscopic scale (Fig. 1b). When pressure on a-rP is reduced below 6.30 GPa, these trends partly reverse leaving the reclaimed sample structure in a more densified configuration. Thermally heating a reclaimed sample seems to completely recover its original structure (see Supplementary Information, Fig. S3).

FSDP ATTRIBUTES SIGNAL VOID-SPACE NETWORK STRUCTURES

If neighbouring subunit structures are pushed apart and yet undistorted by pressure, this suggests the overall MRO chain network must contract sufficiently to account for the 66% increase in density. However, MRO nearest-neighbour lengths decrease by only 3.7–6.8%. A plausible explanation is that significant void-space regions collapse. To gain perspective of atom-void configurations, we created a unique analysis procedure to quantify the void structure of MRO network materials. Here, we define a ‘void’ as a place where it is possible to insert another phosphorus

Table 2 Parameters used to model the void-pixel pair-distribution function, $g(r)_{\text{void}}$ presented in Fig. 4a. The parameters used to model the void-pixel PDFs are given in the first five columns following listed pressures and are: f_v , void fraction; R_p , nominal mean dimension of the single void particle; β , void stretch exponent; R_c , hard-sphere diameter or nominal void spacing; and η , the void packing fraction. Q_{FSDP} is the position of the FSDP in the simulated structure factor with units of \AA^{-1} . The product given by $Q_{\text{FSDP}} R_c$ is essentially constant (1.3% variation) and the product of $Q_{\text{FSDP}} g(r)_{\text{void}}$ is also reasonably constant (7.8% variation), suggesting that indeed the $S(Q)$ FSDP position signals the void-size and void-distribution information.

Pressure (GPa)	$1/f_v$	R_p (\AA)	β	R_c	η (\AA)	$Q_{\text{FSDP}} R_c$	$Q_{\text{FSDP}} g(r)_{\text{void-1st pk}}$
0	9.4	1.30	0	7.0	0.38	6.65	7.30
Elliott							
1.38	19.6	1.06	0	6.2	0.40	6.67	7.60
3.61	49.0	0.82	0	6.0	0.40	6.74	7.70
6.30	769.2	0.38	-0.08	5.6	0.40	6.68	7.57
5.65	625.0	0.40	-0.08	5.6	0.40	6.68	7.72
2.60	400.0	0.40	-0.08	5.8	0.40	6.74	7.76
0	40.3	0.81	0	6.0	0.40	6.64	7.91

atom without displacing existing atoms. Simulation boxes are divided into approximately 10^6 cubic pixels where each pixel is assigned an occupancy value of either 1 or 0. A pixel is classified as ‘occupied’ if it is within a specified distance of any other atoms in the box. This pressure-dependent distance is specified by the first maximum peak position in $g(r)$, r_{max} , assuming the model represents the typical near-neighbour separation of atoms. A void-pixel distribution function results where void size is expressed in units of atomic volume, $1/\rho$ (see Supplementary Information, Fig. S7). Thus, a void of size 1 unit occupies the same volume as that occupied by an atom. The void fraction ratio, f_v , is the number of unoccupied pixels divided by the total number of pixels. Listed in Table 1 are pressure-dependent minimum approach distances and void fractions. Applied pressure naturally reduces the void fraction. There is a remarkable 72% collapse in void fraction between 3.61 and 4.19 GPa. This phenomenon corresponds precisely with the buckling MRO chain network and flattening of P_3 - and/or P_4 -linked structures. For smaller f_v values where void-size dimensions approach the pixel dimension ($\sim 0.3 \text{\AA}$) and where the box consists of less than 1% void pixels, the void fraction becomes more notional and less precise.

The overall void structure is better elucidated by calculating void-pixel PDFs Fig. 4a. Isolated void profiles are not distinguished. The void-size distributions rise to very large values at low r . More importantly, these functions exhibit a very characteristic oscillatory structure, which transmits past the EPSR box edge (Fig. 4a, inset). Therefore, even though the void pixels represent unoccupied space, they can still ‘sense’ the underlying long-range oscillations in atomic number density. These oscillations are present in the PDFs shown in Fig. 2a, but are predominantly masked by the detailed atomic structure. What is remarkable is that they remain detectable even when the void fraction has dropped to $\sim 0.1\%$, so the voids continue to signal these density fluctuations even when greatly diminished, and irrespective of whether or not they span the simulation box. Furthermore, the periodicity of these oscillations varies much more with pressure than atomic oscillations (compare Fig. 4b with Fig. 2c).

The FSDP position correlates well with the void-pixel separation distance given by the first peak in $g(r)_{\text{void}}$. As pressure shifts the FSDP out to larger Q , the first void-pixel peak in this oscillatory function swings to smaller distances. The FSDP area and intensity are found to be linearly proportional to void fraction and electrical resistance (Fig. 4c,d). By extrapolation, we ascertain that the FSDP intensity is fully extinguished when $f_v \leq 0.01\%$. These methods quantify how FSDP attributes are coupled to MRO void-space networks; however, the architecture of isolated void structures remains to be fully elucidated.

CHARACTERIZATION OF VOID STRUCTURE

The excluded volume model⁴⁴ provides a convenient basis to characterize void-space radial distribution functions. We postulate that the voids have a characteristic shape pair-distribution function, and we label this as $g_p(r)$. However, the a-rP void-volume histograms show great diversity in void-size distributions, so any shape function we might introduce must be convoluted with a broad size distribution, thus destroying any shape information it might contain. To mitigate this issue, and better match the observed fall in $g(r)_{\text{void}}$ at low r , we approximated the shape, which includes the size distribution in a mean field sense, to have the form:

$$g_p(r) = \exp \left[- \left(\frac{r}{R_p} \right)^{(1+\beta)} \right].$$

This expression fits calculated $g(r)_{\text{void}}$ PDFs at low r reasonably well, and requires only two adjustable parameters, namely a nominal mean single void dimension, R_p , and a stretch exponent, β , which is useful for very low void fraction situations when the apparent void dimension becomes much smaller than void separations. Thus, the full equation used here to model void-pixel PDFs is given by:

$$g_v(r) = \frac{1}{f_v} g_p(r) + \frac{1}{v_p} \int \mathbf{d}\mathbf{u} g_c(\mathbf{r} - \mathbf{u}) g_p(\mathbf{r}),$$

where $v_p = 4\pi \int_0^\infty r^2 g_p(r) dr$ is the mean void shape function volume, and $g_c(r)$ is the distribution of void centres. We assumed a form for $g_c(r)$ given by the Percus–Yevick hard-sphere radial distribution function⁴⁵ where the void packing fraction, η , is related to the density of voids, ρ_v , and the hard-sphere diameter, R_c , by $\eta = \pi \rho_v R_c^3 / 6$. Here, $g_p(r)$, R_c and η are treated as fitting parameters, although a packing fraction of ~ 0.4 yields reasonable results in all cases tried. Our $g_v(r)$ model parameters used to generate the solid-line curves in Fig. 4a are presented in Table 2.

We find the mean single particle function size, R_p , diminishes steadily with increasing pressure and, concurrently, the mean void-centre separation gradually diminishes. The slightly negative value of β at the smallest void fractions serves to introduce an extended tail to $g_p(r)$. The reason is our hard-sphere PDF produces a very sharp cutoff, whereas real voids will exhibit a much softer overlap. This effect manifests as a mismatch between the model and the EPSR results in the region of 4\AA (Fig. 4a). The products of FSDP line position with the first peak position in $g(r)_{\text{void}}$

and also R_c are nearly constant with pressure, thus providing an unambiguous indication that void-pixel PDFs and modelled void structures properly account for FSDP line positions (Table 2).

A BROADER INTERPRETATION OF MRO IN NETWORK-FORMING MATERIALS

The FSDP of a-rP indicates a structural ordering of atoms that create periodically modulated void structures; from the assembly of atomic subunit structures (triangles, tetrahedra and MRO chain structures) emerge voids with even longer correlation lengths. In monatomic systems such as a-rP, where $S(Q) = S_{NN}(Q)$, the FSDP can only signal the extent of local density fluctuations, and we conclude these arise from voids forming in the structure. The area under the FSDP signals the correlated void fraction. Hence, the porosity of a MRO network material, which is directly proportional to shear modulus and, at least for a-rP, electrical resistivity can be quickly assessed using the FSDP.

The presence of FSDPs from multi-atomic network-forming systems has been attributed to chemical-ordering, where voids result due to correlated directional bonding between pairs of unlike atoms. These claims are not unquestionably proven and, further, they restrict the interpretation of MRO. Using the analysis method described here we could analyse published experimental data spanning the full spectrum of fragile to non-fragile network-forming materials and find that MRO is dominated by local density fluctuations. In this instance, the interpretation of MRO is not restricted by chemical ordering and hence lends itself to more wide-ranging and robust structural characterizations. For example, the FSDP can indicate structural ordering that will enable, with less geometrical bonding restrictions, the creation of elegant ionic structure models, which in turn will accurately characterize useful functionalities (for example, mass diffusion, fragility, magnetic, electron transport and so on) of natural or *in silico* designed binary network glasses. The tools we present here, which definitively elucidate the atomic-void structures of disordered materials, will enable more systematic approaches towards the development of countless useful products and resources.

METHODS

METHODS SUMMARY

A <1 g lump of 99.9999% pure a-rP was polished to yield 50- μm -thick plates, which were cut into $\sim 100\ \mu\text{m}$ square samples. Angle-dispersive X-ray diffraction data were collected on beamline 12.2.2 of the Advanced Light Source (35 keV). A specially designed diamond anvil was inserted into a modified high-pressure cell to permit smoothly varying diffraction intensities up to $110^\circ 2\theta$. Background and sample data were collected to 6.30 GPa. Two-dimensional diffraction images were radially integrated to render angularly dependent scattering intensities. Total scattering structure factors $S(Q)$ were determined by subtracting background scattering contributions due to air, diamond windows, the pressure medium and temperature diffuse scattering^{46–48}. The measured fluid-pressure-medium intensity background contribution is a factor of three times higher when compared with a-rP sample intensity data; there is only fluid above the sample. However, comparison to ambient-pressure P–P–P inclusion angle results clearly indicates that the fluid-pressure-medium overcorrection does not affect the integrity of our 3D model. The $S(Q)$ data were Fourier transformed to yield electron density structure factors $F(r)$. Sample density was determined at each pressure from the intra-atomic region of $F(r)$ using the method of Eggert *et al.*⁴⁸. One improvement here is the use of corresponding high-pressure background data. Density was computed for each pressure by averaging 20 values over $S(Q) = 8–10\ \text{\AA}^{-1}$. Averaged results are reported with error bars corresponding to standard deviations (Table 1). Atomic structural models were refined using EPSR (ref. 43). $S(Q)$ data, density, an approximate interatomic potential and estimated bond distances constrain EPSR computations. The initial potential is perturbed until a satisfactory fit to the diffraction data is obtained. Raman spectra were collected using a Horiba JY 0.3 m LabRAM system (1,800 grooves mm^{-1} grating) using continuous-wave

output from a HeNe laser (632.8 nm). A back-illuminated liquid-nitrogen-cooled CCD (charge-coupled device) detector captured the Raman scattered photons. Raman spectra were collected below the damage threshold fluences given in Supplementary Information, Fig. S8. Below 3.5 GPa, between 40 and 60 separate time exposures were collected over spatially different positions. These spectra were averaged to generate each pressure-dependent spectrum.

SAMPLE

Our 99.9999% pure a-rP was obtained from Alfa Aesar Puratonic. One <1 g lump of material was polished to a 50 μm flat plate using Al_2O_3 paper. The sample was then cut into $100 \times 100\ \mu\text{m}$ sections. The ambient condition density was determined by helium pycnometry. Three trials were run and the average value was determined to be $2.137 \pm 0.103\ \text{g cm}^{-3}$. Raman (LLNL), X-ray (LBNL-ALS) and neutron diffraction patterns (LANL-LANSCE) were collected and found to be very similar to those in the literature^{10,11,20–24,31–34}.

X-RAY DIFFRACTION DATA

X-ray diffraction data were collected on beamline 12.2.2 at the Advanced Light Source, Lawrence Berkeley National Laboratory. This is a modern brightness preserving high-pressure beamline⁴⁹. The beamline benefits from X-radiation generated by a 6 GeV superbend magnet. Monochromatic radiation is selected using a two-bounce Si 111 monochromator. X-rays are initially focused using a toroidal mirror and then further focused using KB mirrors to give a $10 \times 10\ \mu\text{m}$ X-ray spot. A MAR 345 image plate detector collected diffraction images.

A custom-designed diamond anvil cell (DAC) built to enable X-ray diffraction out to very high angles was used in our study. This DAC consists of a four-post symmetrical design with WC Boehler-Almax type backing plates and a 1.7-mm-tall, 6.5-mm-girdle-diameter, type-IB diamond on the downstream side and a conventional backing plate and diamond on the upstream side. This combination enables diffraction data to be collected at angles of up to $110^\circ 2\theta$. Scattering intensity varies smoothly as X-rays traverse only through air, the sample and diamond windows. The minimum sample-to-detector distance available on BL 12.2.2 is 135 mm, which combined with the highest useful energy of 35 keV limited the maximum Q -range to $\sim 10\ \text{\AA}^{-1}$. A rhenium gasket radially confined the sample, pressure manometer and pressure medium. The original foil thickness was 250 μm and this was pressed to 70 μm before a 220 μm hole was cut using a micro-electrical discharge machine purchased from Hylozoic Products. The a-rP was loaded into the pressure cavity together with NaCl and strontium tetraborate pressure manometers. The pressure-transmitting fluid consisted of a 4:1 mixture of methanol/ethanol (see Supplementary Information, Fig. S9). According to high-pressure ultrasonic studies conducted over the same pressure range of this study, the alcohol fluid compressibility exceeds that of a-rP. At low pressure, it is conceivable that the pressure medium permeates the a-rP void space. We found no experimental evidence supporting the notion that a-rP chemically reacts with the pressure-transmitting fluid. Materials were loaded to permit spatially discrete measurements of a-rP, manometers and the alcohol pressure medium. This data collection sequence was repeated at each pressure reported in our study.

RAMAN SPECTROSCOPY DATA

Raman spectra were collected on a JY 0.3 m LabRam system using continuous-wave laser 632.8 nm radiation. Spectral calibration was made using a neon lamp. The laser excitation spot size was nominally 2–4 μm . Strontium tetraborate was used as an optical pressure manometer. The sample was compressed using a symmetrical DAC (piston-cell design by P. Pruzan) comprising type-II synthetic diamonds (Sumitomo Electric Ind. Ltd) with 0.4 mm culets. The sample was radially constrained by a rhenium gasket with a 65–70- μm -thick sample chamber and a diameter of nominally 220 μm . A 4:1 methanol/ethanol mixture was used as a pressure-transmitting fluid as it is purely hydrostatic over the pressure range of this study (see Supplementary Information, Fig. S9). Raman data were collected with identical time exposures from the pressure medium, Re gasket and a-rP. At 6.60 GPa, in the absence of shear forces, a-rP begins to slowly (72 or more hours) transform to rhombohedral black phosphorus (see Supplementary Information, Fig. S6a,b). Raman spectra were collected along compression and decompression paths. The gasket spectrum provided the instrument response function that was subtracted from both sample and background spectra. The magnitude of pressure-medium contributions to a-rP spectra were determined by comparing the O–H and C–H mode intensities. In this way, the spectral contributions of the fluid pressure medium were systematically eliminated from each a-rP spectrum.

Our laser excitation wavelength essentially matched the ambient condition optical gap of a-rP, 1.96 eV, so particular attention had to be paid to prevent photolysis reactions due to excessive laser fluence. We found that the damage threshold increased going from 457 to 632.8 nm wavelengths. At ambient pressure, the 632.8 nm laser power had to be kept below 50 μ W and exposure time less than 5–10 s. All reported a-rP spectra collected below 3 GPa consist of an average of between 40 and 60 time exposures collected over spatially separate positions (compression cycle data are presented in Supplementary Information, Fig. S2a,c). The Raman intensity dropped by 10^2 from 0 to 3.5 GPa (Fig. 3d). From 3.61 to 6.60 GPa, the optical damage threshold steadily increased to the point where 8 mW laser power could be used with significantly longer time exposures (see Supplementary Information, Fig. S8). These trends partially reversed when pressure was released. Pressure was completely released and the reclaimed sample Raman spectrum was not exactly the same as the original sample. More importantly, we discovered that we could completely restore the reclaimed a-rP Raman spectral features by heating to approximately 573 K (see Supplementary Information, Fig. S3).

Each spectrum was fitted by a sum of Voightian peak shape functions using a least-squares procedure (see Supplementary Information, Fig. S2b,c). A sample was immersed in liquid nitrogen at ambient pressure to improve the spectral resolution of individual peaks (see Supplementary Information, Fig. S2c). This enabled us to confirm the suspected presence of the weak Raman modes at ambient temperature. These peaks were then fitted to our ambient-temperature and high-pressure data using the same method. As pressure increased, the spectra became more convoluted; hence, previous fit parameters were used as initial guess values for the subsequent higher-pressure fit.

USING EPSR TO REFINE 3D STRUCTURAL MODELS

To ensure complete removal of background contributions to $S(Q)$, the data were smoothed with a square-wave function (SWF) and the result is subtracted from the original source of data. This residual $S(Q)$ was then transformed to r -space. Analytical deconvolution of the smoothing function was carried out in r -space by dividing the Fourier-transformed residual by the analytical Fourier transform of the SWF, at the same time enforcing the requirement that $g(r) = 0$ for $r < 1.6 \text{ \AA}$. The deconvoluted $g(r)$ was then Fourier transformed back to Q -space. A SWF has an analytic Fourier transform; hence, the Fourier transform of this convolution in Q -space (approaches zero at high Q) becomes the product of Fourier transforms in r -space. Consequently, this procedure does not degrade the Q resolution nor does it introduce truncation oscillations in r -space.

In each case, a box of 2,000 atoms was built with a volume determined from the respective densities listed in Table 1. Each P atom was given a Lennard-Jones σ value of 2.2 \AA and an ϵ value of 0.5 kJ mol^{-1} . The interaction potential was extended out to $r = 18 \text{ \AA}$. In addition to the experimental data, a further constraint on the minimum approach P–P distance of 1.8 \AA was applied. The absolute energy from the empirical potential was allowed to rise to $\sim 100\text{--}200 \text{ kJ mol}^{-1}$, depending on the density and data. Comparisons between EPSR and experiment are quite favourable over the full pressure range (Fig. 1c,d).

At the outset, there is no guarantee that a 3D arrangement of atoms can be found that fits the diffraction data and that at the same time satisfies other constraints such as minimum approach distances and the overall density. That such an arrangement exists is obvious because the material exists, but whether we can find it, and whether the one we find is the correct one are questions that do not have a simple answer. This is not a sufficient condition on the structure, but it is certainly a necessary one, that would not be satisfied for example if we simply Fourier transform diffraction data to real space. The EPSR method requires reasonable assumptions about minimum approach distances and likely interactions between atoms, and then perturbs those interactions in such a way as to produce as close a fit to the diffraction data as is practical. As the data—structure factors—are purely pair-wise additive, then the resulting effective interaction potentials are also pair-wise additive. This may be a problem if the many-body forces are important, which they probably are in this case, but equally it does not automatically imply that the equilibrated structure is incorrect.

Received 9 January 2008; accepted 12 September 2008; published 12 October 2008.

References

- Tawada, Y., Tsuge, K., Kondo, M., Okamoto, H. & Hamakawa, Y. Properties and structure of alpha-SiC-H for high-efficiency alpha-Si solar-cell. *J. Appl. Phys.* **53**, 5273–5281 (1982).
- Kalkhoran, N. M., Namavar, F. & Maruska, H. P. Optoelectric applications of porous polycrystalline silicon. *Appl. Phys. Lett.* **63**, 2661–2663 (1993).
- Kohara, S. *et al.* Structural basis for the fast change of Ge₂Sb₂Te₅: Ring statistics analogy between the crystal and amorphous states. *Appl. Phys. Lett.* **89**, 201910 (2006).
- Wang, Y., Li, J., Hamza, A. V. & Barbee, T. W. Ductile crystalline line-amorphous nanolaminates. *Proc. Natl Acad. Sci.* **104**, 11155–11160 (2007).
- Lucovsky, G. Specification of medium range order in amorphous materials. *J. Non-Cryst. Solids* **97**, 155–158 (1987).
- Popescu, M. A. Hole structure of computer models of non-crystalline materials. *J. Non-Cryst. Solids* **35**, 549–554 (1980).
- Elliott, S. R. Medium range order in covalent amorphous solids. *Nature* **354**, 445–452 (1991).
- Bhatia, A. B. & Thorton, D. E. Structural aspects of the electrical resistivity of binary alloys. *Phys. Rev. B* **2**, 3004–3012 (1970).
- Elliott, S. R. Origin of the first sharp diffraction peak in the structure factor of covalent glasses. *Phys. Rev. Lett.* **67**, 711–714 (1991).
- Lannin, J. S. & Shanabrook, B. V. Intermediate range order in amorphous red phosphorus. *J. Non-Cryst. Solids* **49**, 209–218 (1982).
- Lannin, J. S. & Shanabrook, B. V. Raman scattering and infrared absorption in amorphous red phosphorus. *Solid State Commun.* **28**, 497–500 (1978).
- Shanabrook, B. V., Lannin, J. S. & Taylor, P. C. Far infrared absorption in bulk amorphous red phosphorus. *Solid State Commun.* **32**, 1279–1283 (1979).
- Goodman, N. B., Ley, L. & Bullett, D. W. Valence-band structures of phosphorus allotropes. *Phys. Rev. B* **27**, 7440–7450 (1983).
- Wilson, M. & Madden, P. A. Voids, layers, and the first sharp diffraction peak in ZnCl₂. *Phys. Rev. Lett.* **80**, 532–535 (1988).
- Fowler, T. G. & Elliott, S. R. Continuous random network models for a-As₂S₃. *J. Non-Cryst. Solids* **92**, 31–50 (1987).
- Susman, S., Volin, K. J., Montague, D. G. & Price, D. L. Temperature dependence of the first sharp diffraction peak in vitreous silica. *Phys. Rev. B* **43**, 11/076–081 (1991).
- Višćor, P. Structure and the existence of the first sharp diffraction peak in amorphous germanium prepared in UHV and measured in-situ. *J. Non-Cryst. Solids* **97**, 179–182 (1987).
- Vepřek, S. & Beyeler, H. U. On the interpretation of the first, sharp maximum in the X-ray scattering pattern of non-crystalline solids and liquids. *Phil. Mag. B* **44**, 557–567 (1981).
- Wilson, M., Madden, P. A., Medvedev, N. N., Geiger, A. & Appelhagen, A. Voids in network forming liquids and their influences on the structure and dynamics. *J. Chem. Soc. Faraday Trans.* **94**, 1221–1228 (1998).
- Hultgren, R., Gingrich, N. S. & Warren, B. E. The atomic distribution in red and black phosphorus and the crystalline structure of black phosphorus. *J. Chem. Phys.* **3**, 351–355 (1935).
- Krebs, H. & Gruber, H. U. The atomic distribution in glassy red phosphorus. *Z. Naturf.* **22a**, 96–102 (1967).
- Tsvignov, A. N. X-ray study of the allotropic conversions of amorphous red phosphorus at high pressure and temperature. *Russ. J. Phys. Chem.* **51**, 1331–1333 (1979).
- Durig, J. R. & Casper, J. M. On the vibrational spectra and structure of red phosphorus. *J. Mol. Struct.* **5**, 351–358 (1970).
- Olego, D. J. *et al.* The microscopic structure of bulk amorphous red phosphorus: A Raman scattering investigation. *Solid State Commun.* **52**, 311–314 (1984).
- Shanabrook, B. V., Bishop, S. G. & Taylor, P. C. Photo-luminescence and electron-spin-resonance studies of localized states in amorphous phosphorus. *J. Physique* **42**, C4–C865 (1981).
- Long, L. J., Guarise, G. B. & Marani, A. Phase transitions of phosphorus at high pressure. *Corsi. Semin. Chim.* **5**, 97–104 (1967).
- Extance, P. & Elliott, S. R. Pressure dependence of the electrical conductivity of amorphous red phosphorus. *Phil. Mag. B* **43**, 469–483 (1980).
- Sorgoto, L., Guarise, G. B. & Marini, A. Red to black phosphorus transition up to 65 kbar. *High Temp.–High Pressures* **2**, 405–411 (1970).
- Phillips, R. T. & Sobiesierski, Z. Recombination in amorphous red phosphorus. *J. Phys. C* **20**, 4259–4269 (1987).
- Depinna, S. & Cavennet, B. C. Radiative recombination in amorphous phosphorus. *J. Phys. C* **16**, 7063–7080 (1983).
- Elliott, S. R., Dore, J. C. & Marseglia, E. The structure of amorphous phosphorus. *J. Phys. Colloq.* **46**, C8–C349 (1985).
- Farmen, H., Blakely, D., Dore, J. C., Bellissent-Funel, M.-C. & Elliott, S. R. Neutron diffraction studies of network structures in amorphous phosphorus. *Phys. Scr.* **49**, 634–636 (1994).
- Jones, R. O. & Hohl, D. Structure of phosphorus clusters using simulated annealing—P₂ to P₈. *J. Chem. Phys.* **92**, 6710–6721 (1990).
- Jóvári, P. & Pusztai, L. On the structure of amorphous red phosphorus. *Appl. Phys. A* **74**, S1092–S1094 (2002).
- Jürgensen, A. The P(1s) and P(2p) XAFS spectra of elemental phosphorus, theory and experiment. *Phys. Scr.* **T115**, 548–551 (2005).
- Ruck, M. *et al.* Fibrous red phosphorus. *Angew. Chem. Int. Ed.* **44**, 7616–7619 (2005).
- Fasol, G., Cardona, W., Hönle, W. & v Scherner, H. G. Lattice dynamics of Hittorf's phosphorus and identification of structural defects in amorphous phosphorus. *Solid State Commun.* **52**, 307–310 (1984).
- Jones, R. O. & Hohl, D. Structure of phosphorus clusters using simulated annealing P₂ to P₈. *J. Chem. Phys.* **92**, 6710–6721 (1990).
- Hohl, D. & Jones, R. O. Amorphous phosphorus: A cluster-network model. *Phys. Rev. B* **45**, 8995–9005 (1992).
- Böcker, S. & Häser, M. Covalent structures of phosphorus: A comprehensive theoretical study. *Z. Anorg. Allg. Chem.* **621**, 258–286 (1995).
- Song, B., Cao, P.-L., Zhao, W. & Li, B.-X. The structure of P₈ and P₉ clusters. *Phys. Status Solidi. B* **226**, 305–314 (2001).
- Greaves, G. N., Elliott, S. R. & Davis, E. A. Amorphous arsenic. *Adv. Phys.* **28**, 49–141 (1979).
- Soper, A. K. Partial structure factors from disordered materials diffraction data: An approach using empirical potential structure refinement. *Phys. Rev. B* **72**, 104204 (2005).
- Soper, A. K. The excluded volume effect in confined fluids and liquid water. *J. Phys. Condens. Matter* **9**, 2399–2410 (1997).
- Percus, J. K. & Yevick, G. J. Analysis of classical statistical mechanics by means of collective coordinates. *Phys. Rev.* **110**, 1–13 (1958).
- v Zernike, F. & Prins, J. A. X-ray diffraction to determine molecular structure in fluids. *Z. F. Phys.* **41**, 184–194 (1927).
- Debye, P. X-ray scattering. *Ann. Phys. (Leipzig)* **46**, 809–823 (1915).
- Eggert, J. H., Weck, G., Loubeyre, P. & Mezouar, M. Quantitative structure factor and density measurements of high-pressure fluids in diamond anvil cells by x-ray diffraction: Argon and water. *Phys. Rev. B* **65**, 174105 (2002).
- Kunz, M. *et al.* A beamline for high pressure studies at the Advanced Light Source with a superconducting bending magnet as the source. *J. Synchrotron. Radiat.* **12**, 650–658 (2005).

Supplementary Information accompanies the paper at www.nature.com/naturematerials.

Acknowledgements

J.M.Z. thanks J. Molitoris for sparking an interest to study a-rP, M. Bastea for providing a-rP sample material and C. Thompson of www.mathengineering.com for Matlab consulting and code acceleration tips. We thank J. Eggert for his guidance to properly determine density from high-pressure diffraction data. This work was carried out under the auspices of the US Department of Energy jointly by Lawrence Livermore National Laboratory under Contract DE-AC52-07NA27344. The Advanced Light Source is supported by the Director, Office of Science, Office of Basic Energy Sciences, of the US Department of Energy under Contract DE-AC03-76SF00098.

Author contributions

J.M.Z. devised the project and design engineered the ultrawide-aperture DAC. J.M.Z. and S.M.C. conducted X-ray experiments and subsequent data reductions. J.M.Z. conducted micro-Raman scattering experiments and corresponding data analysis. A.K.S. carried out EPSR analysis of diffraction data. J.M.Z. and A.K.S. wrote the manuscript.

Author information

Reprints and permissions information is available online at <http://npg.nature.com/reprintsandpermissions>. Correspondence and requests for materials should be addressed to J.M.Z.